SANDIA REPORT
SAND2021-12278
Printed September 2021

Sandia National Laboratories

Code Development Supporting a Non-Thermal Source of High Fluence Warm X-Rays

Nichelle Bennett and Dale R. Welch

Prepared by
Sandia National Laboratories
Albuquerque, New Mexico 87185
Livermore, California 94550

Issued by Sandia National Laboratories, operated for the United States Department of Energy by National Technology & Engineering Solutions of Sandia, LLC.

Available to DOE and DOE contractors from

U.S. Department of Energy
Office of Scientific and Technical Information
P.O. Box 62
Oak Ridge, TN 37831

Telephone: (865) 576-8401
Facsimile: (865) 576-5728
E-Mail: reports@osti.gov
Online ordering: http://www.osti.gov/scitech

Available to the public from

U.S. Department of Commerce
National Technical Information Service
5301 Shawnee Road
Alexandria, VA 22312

Telephone: (800) 553-6847
Facsimile: (703) 605-6900
E-Mail: orders@ntis.gov
Online order: https://classic.ntis.gov/help/order-methods

ABSTRACT

A six-month research effort has advanced the hybrid kinetic-fluid modeling capability required for developing non-thermal warm x-ray sources on Z. The three particle treatments of quasi-neutral, multi-fluid, and kinetic are demonstrated in 1D simulations of an Ar gas puff. The simulations determine required resolutions for the advanced implicit solution techniques and debug hybrid particle treatments with equation-of-state and radiation transport. The kinetic treatment is used in preliminary analysis of the non-Maxwellian nature of a gas target. It is also demonstrates the sensitivity of the cyclotron and collision frequencies in determining the transition from thermal to non-thermal particle populations. Finally, a 2D Ar gas puff simulation of a Z shot demonstrates the readiness to proceed with realistic target configurations. The results put us on a very firm footing to proceed to a full LDRD which includes continued development transition criteria and x-ray yield calculation.

Acknowledgment

The author wishes to thank Christopher Jennings for providing the 2D density distributions for the Ar gas puff. Dr. Jennings and Roger Vesey were generous with their time for discussions regarding gas puff dynamics and warm x-ray sources.

CONTENTS

LIST OF FIGURES

0.1. Introduction

Z-pinch implosions on Sandia's Z Machine are efficient sources of warm x-rays from thermal K-shell Heα and Lyα emission[14, 23, 13, 2, 1, 24, 28]. For example, Ar gas puffs generate $\sim$ 3.3 keV photons with a peak yield of $\sim$ 350 kJ and Al wire arrays generate $\sim$ 3.3 keV photons with a peak yield of 375 kJ [12]. This report addresses the effort to extend the spectral range of Sandia's warm x-ray sources.

Thermal emission becomes less efficient as the x-ray energies exceed the plasma temperature (2.5 keV), with published yields above 15 keV of less than 10 kJ [12]. This is seen in the yields from various warm x-ray source materials versus energy from Ref. [1], included for reference here in Fig. 0-1. Non-thermal warm x-ray emission scales more favorably with x-ray energy, as shown in Fig. 0-2, which is reproduced from Ref. [3]. In non-thermal emission, a higher-Z material is weakly ionized, retaining most of its inner shell electrons. Particle impact ionization strips an electron from the 1s orbital state, which is subsequently filled by an electron from the 2p state. The resulting "cold Kα" x-ray emission suffers less radiative losses from heating and ionization than thermal emission.

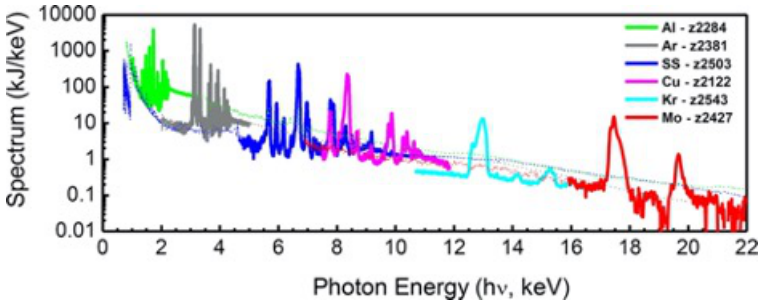

Figure 0-1. The yields from various warm x-ray source materials versus energy from Ref. [1]. The yield is binned in kJ/keV.

While non-thermal x-rays have been measured on Z and non-thermal production would extend our spectral reach, we need the tools to model this process. The magnetohydrodynamic (MHD) codes [17, 32] used are fast but lack non-thermal physics. We are developing a hybrid modeling capability that uses the fast features of MHD-type particles to the greatest extent possible, then transitions to slower but more complete particle treatments to correctly capture the particle energy spectra that generate non-thermal emission. This capability is founded on the fully-relativistic particle-in-cell (PIC) code CHICAGO, which already features hybrid fluid-kinetic modeling [36, 7, 5, 33, 26]. The fluid and kinetic particle treatments are reviewed in Sec. 0.2 and the transitions techniques between these treatments are described in Secs. 0.5 and 0.6.

This six-month research effort focused on a model of an Ar gas puff [20] accomplishing four tasks. First, the gas-puff pinch is modeled in 1D separately for the non-transitioning quasi-neutral, multi-fluid, and kinetic treatments. Convergence studies with these simulations determine the spatial and temporal resolutions required. These results, presented in Sec. 0.3, may be applied to the implosion phase. The relatively large radius of a gas-puff target makes a larger grid size than found in liner-type targets. The grid is most efficiently constructed of variable size

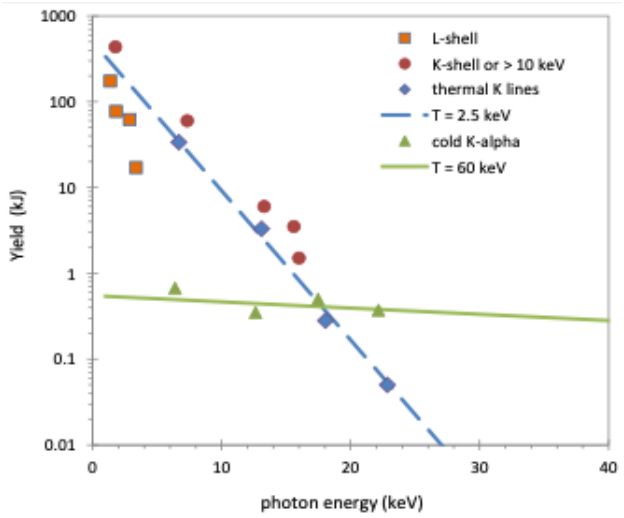

Figure 0-2. Warm x-ray yields as a function of photon energy from thermal (blue) and non-thermal (green) sources on Z. (Figure reproduced from Ref. [3].)

with the highest resolution confined to the region of the pinch. The pinch resolution will be determined in a follow-on study.

For the second task, multiple kinetic 1D simulations, with $\bar{Z}$ initialized to 1, 2, and 6, provide the most realistic transport and demonstrate the energy and spatial distributions for interpenetrating electrons and ions. These also demonstrate the utility of the Hall parameter as a transition criterion. However, they necessitate additional convergence studies due to the increase in electron population with the initialized $\bar{Z}$. This is in addition to determining the required resolution in the pinch region and the viability of other transition criteria, such as the Dreicer field [15, 16]. The kinetic dynamics are discussed in Sec. 0.4.

The third task uses the resolutions determined from the first task. Simulations are initialized as quasi-neutral and multi-fluid and successfully transitioned to multi-fluid and kinetic, respectively. This required code improvements to match the electron-ion species pairs and debugging in the equation of state (EOS) algorithm. The code modification are briefly discussed in Sec. 0.5. The results of the particle-treatment transitions are then discussed in Sec. 0.6.

Lastly in Sec. 0.7, realistic 2D Ar density distributions are used to initialize a 2D gas puff simulation to test run time and stability. This test is in progress.

The results put us on a very firm footing to proceed to a full LDRD which includes continued model development for transitions in the particle treatment and warm x-ray yield calculation.

0.2. Particle equations of motion in the hybrid PIC code CHICAGO

The fundamental equations governing particle and field propagation are the Lorentz force on an individual particle and Maxwell's equations:

$$
\begin{aligned}
m_\alpha \frac{d(\gamma_\alpha \mathbf{v}_\alpha)}{dt} &= q_\alpha(\mathbf{E}+\mathbf{v}_\alpha\times\mathbf{B}) - \nu_{\alpha\beta} m_\alpha(\mathbf{v}_\alpha - \mathbf{v}_\beta) && (0.1)\\
\varepsilon\mu\frac{\partial \mathbf{E}}{\partial t} &= \nabla\times\mathbf{B} - \mu\mathbf{j} && (0.2)\\
\frac{\partial \mathbf{B}}{\partial t} &= -\nabla\times\mathbf{E} && (0.3)\\
\nabla\cdot\mathbf{E} &= \frac{\rho_e}{\varepsilon} && (0.4)\\
\nabla\cdot\mathbf{B} &= 0.
\end{aligned}
$$

PIC codes typically solve Eqs. 0.2 through 0.4 for the fields. Eq. 0.1 is the equation of motion for kinetic particles, where ν_{ij} is the collision frequency. This collision term may be replaced by a binary collision model. The Coulomb collision frequency is supplied by Spitzer for species α scattering off species β [27]:

$$
\nu_{\alpha\beta} = \frac{4\sqrt{2\pi}e^4 Z_\alpha^2 Z_\beta^2 n_\beta \ln\Lambda_{\alpha\beta}}{(4\pi\varepsilon_0)^2\, 3 m_\alpha m_{\alpha\beta}} \left(\frac{T_\alpha}{m_\alpha} + \frac{T_\beta}{m_\beta}\right)^{-3/2}, \qquad (0.5)
$$

where $m_{\alpha\beta} = m_\alpha m_\beta/(m_\alpha + m_\beta)$ and $\ln\Lambda_{\alpha\beta}$ is the Coulomb logarithm.

In the kinetic treatment, the electron cyclotron frequency (ω_{ce}) and plasma frequency (ω_{pe}) must be resolved to some level to capture the collisions and orbits generated by Eq. 0.1. The required ω_{ce} and ω_{pe} resolution are determined by the specific implicit technique used in the particle push. The value of $\omega_{ce}\Delta t = 1.5$ that is used in simulations in this report is enabled by the Magnetic Implicit solution in CHICAGO [18, 34]. Still, high combined spatial and charge resolution is required in the kinetic simulations due to the artificial collisionality inherent in an energy-conserving algorithm. This artificial collisionality is reduced by a cloud-in-cell treatment [8, 35]. In a previous SAND report, we noted that energy and momentum conservation require a grid resolution related to the electron collisionless skin depth, $l_s = c/\omega_p$ [26]. A value of $\Delta x = 6 l_s$ was stable for densities $10^{16} - 10^{19}$ cm^{-3}. Code issues that are under investigation include 1) the maximum allowable $\omega_{ce}\Delta t$, 2) the nature of the artificial collisionality, and 3) the most stable cloud-in-cell function.

In addition to the kinetic particle treatment typical of PIC codes, CHICAGO includes fluid treatments for particles, modifying Eq. 0.1 (with particle energy equations) while retaining Eqs. 0.2 through 0.4. This is possible because particles are separate entities from the grid cells. The multi-fluid treatment, or inertial fluid, available in CHICAGO is the most similar to kinetic and has the same spatial resolution requirements. This is because the equation of motion for inertial fluids is identical to kinetic with the addition of the pressure term which describes intra-species collisions [33]. The standard collision term is retained for inter-species scattering. The equations

of motion for electron and ion species, without the thermal force, are [36, 30, 33]

$$\begin{aligned} m_e \frac{d\mathbf{v}_e}{dt} &= -e\left(\mathbf{E} + \frac{\mathbf{v}_e}{c} \times \mathbf{B}\right) - \frac{\nabla p_e}{n_e} - m_e \nu_{ei}(\mathbf{v}_e - \mathbf{v}_i), \\ m_i \frac{d\mathbf{v}_i}{dt} &= e\bar{Z}\left(\mathbf{E} + \frac{\mathbf{v}_i}{c} \times \mathbf{B}\right) - \frac{\nabla p_i}{n_i} - m_i \nu_{ij}(\mathbf{v}_i - \mathbf{v}_j), \end{aligned} \tag{0.6}$$

The inertial fluid model avoids numerical cooling by including a separate equation for particle energy. The electron and ion internal energies advance using [29, 33]

$$\begin{aligned} \frac{dU_\alpha}{dt} &= -\frac{p_e \nabla \cdot \mathbf{v}_\alpha}{n_\alpha} + \frac{\nabla \cdot (\kappa_e \nabla T_\alpha)}{n_\alpha} + \sum_\beta \nu_{\alpha\beta} \frac{m_\alpha m_\beta}{m_\alpha + m_\beta} (\mathbf{v}_\beta - \mathbf{v}_\alpha)^2 \\ &\quad + \sum_\beta \frac{3 m_\alpha \nu_{\alpha\beta}}{m_\alpha + m_\beta} (T_\beta - T_\alpha) + \dot{E}_{rad}. \end{aligned} \tag{0.7}$$

The last term accounts for emission/absorption of radiation when an EOS treatment is used. Viscosity terms may be added to Eq. 0.6 and Ref. [30] suggests this is useful to avoid numerical problems at shock fronts. The viscosity tensor is part of the suite of classical transport coefficients along with electrical conductivity, thermal conductivity, and thermoelectric coefficients [10, 4, 9]. It is represented as [9]

$$\Pi^\alpha_{kl} = -\mu^\alpha_{klmn} \nu_{mn} \tag{0.8}$$

where Π^α is the pressure tensor for species α, μ^α_{klmn} is the viscosity tensor for species α, and

$$\nu_{mn} = \frac{\partial v_n}{\partial x_m} + \frac{\partial v_m}{\partial x_n} - \frac{2}{3} \delta_{mn} \nabla \cdot \mathbf{v}.$$

The maximum values for the viscosity coefficients are determined by the simulation spatial and temporal resolution. For electrons, $\mu^e_{max} = 0.5\Delta x^2/\Delta t$, and for ions, $\mu^i_{max} = (m_i/m_e)\mu^e_{max}$.

While the kinetic treatment is typically the most accurate, multi-fluid particles have the advantage of faster simulation run times for a few reasons. First, collisions within a species are not modeled but are assumed to obey a Maxwell distribution. This, in turn, enables the number of particles, or charge resolution, to be reduced, particularly when the Eulerian remap is used. Third, an EOS treatment is available for multi-fluid in which the electron and ion charge-to-mass is adjusted based on $\bar{Z}$.

The quasi-neutral treatment [30, 31] is the fastest of the three and enjoys a lower resolution requirement because electron inertia is neglected. In the quasi-neutral model, the assumption is $\rho_e \sim 0$ or, equivalently,

$$n_e = \sum_{k=1}^{N_i} \bar{Z} n_k,$$

where Z_k is the charge state of the kth ion. Therefore, it is possible to follow an ion macroparticle which carries the fluid information for the inertia-less electrons (which have no equation of

motion). This treatment most closely resembles MHD. The equation of motion for the composite ion-electron macroparticle is [30]

$$m_i n_i \frac{d\mathbf{v}}{dt} = \mathbf{j} \times \mathbf{B} - \nabla(p_e + p_i), \tag{0.9}$$

where p_e is the electron pressure. When multiple quasi-neutral ion species are modeled, the current becomes [30]

$$\mathbf{j} = \sigma \left[\mathbf{E} + \mathbf{v}_+ \times \mathbf{B} - \frac{1}{en_e}(\nabla p_e + \beta \nabla T_e) - \frac{m_e}{e} \sum_{k=1}^{N_i} \nu_{ek}(\mathbf{v}_k - \mathbf{v}_+) \right]$$

where

$$\mathbf{v}_+ = \sum_{k=1}^{N_i} \rho_k \mathbf{v}_k$$

and

$$\rho_k = \frac{\bar{Z} n_k}{n_e}.$$

The current is substituted for the electric field such that the MHD multi-ion momentum equations are

$$\begin{aligned} m_i n_i \frac{d\mathbf{v}_k}{dt} &= \rho_k \mathbf{j} \times \mathbf{B} - \nabla p_k - \rho_k \nabla p_e + \rho_k \beta n_e \nabla T_e \\ &\quad - n_k m_k \sum_{k=1}^{N_i} \nu_{kl}(\mathbf{v}_k - \mathbf{v}_l) \\ &\quad - n_e m_e \nu_{ek}(\mathbf{v}_k - \mathbf{v}_+) + e n_e \rho_k \nu_{ek}(\mathbf{v}_k - \mathbf{v}_+) \times \mathbf{B} \\ &\quad + \rho_k n_e m_e \sum_{k=1}^{N_i} \nu_{el}(\mathbf{v}_l - \mathbf{v}_+) + \frac{m_e}{e}(\rho_k \nu_e - \nu_{ek})\mathbf{j} \end{aligned} \tag{0.10}$$

The fields, currents, densities, and electron pressure gradient are all calculated at the nodes and then interpolated to the macroparticle position when Eq. 0.9 is applied.

0.3. Ar gas puff 1D models for each particle treatment

Simulations are first conducted in 1D without transitions to separately exercise the particle equations of motion described in Sec. 0.2. One goal is to identify the spatial and temporal resolution necessary for each treatment to remain numerically stable during implosion. A second goal is to verify the EOS and radiation transport implementation. All identified code issues are resolved, with details provided in Sec. 0.5.

The 1D simulations use a simple linear pulse rise, which is unrealistically fast. The peak current of 15.5 MA is reached in 69 ns. The initial distribution of gas density is more realistic, taken from the two-jet configuration published in Ref. [24]. This distribution is plotted in Fig. 0-3a.

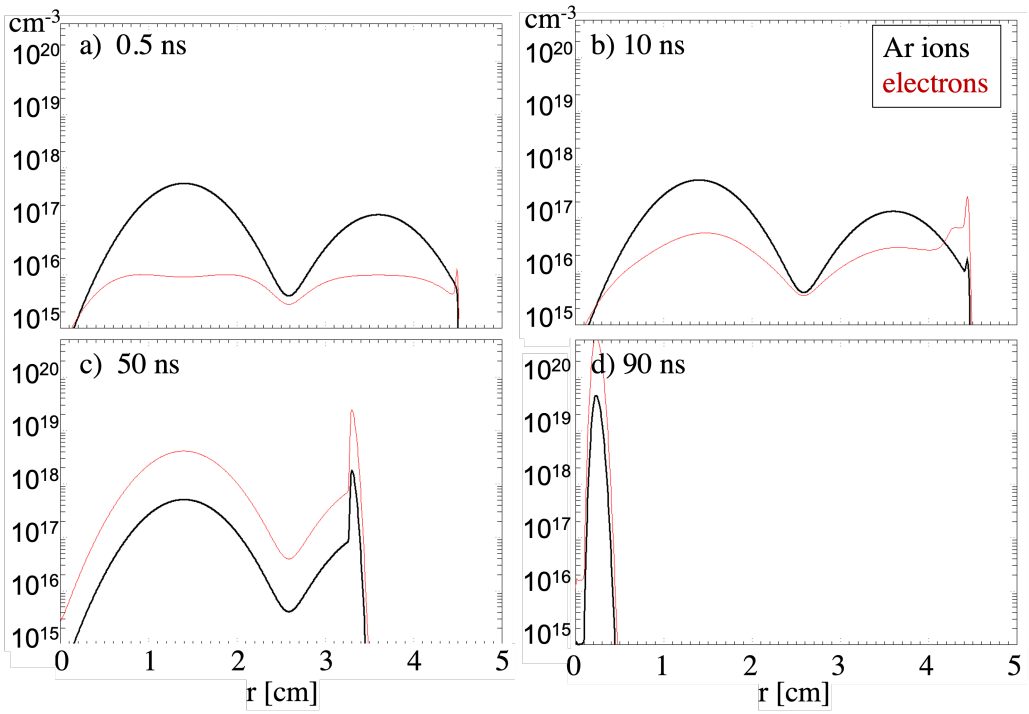

Figure 0-3. The evolution of Ar ion and electron densities in a 1D quasi-neutral simulation. The density distributions are shown separately for ions (black) and electrons (red) at four times during the pinch: a) 0.5, b) 10, c) 50, and d) 90 ns.

The quasi-neutral and multi-fluid versions use an EOS treatment, which is possible in CHICAGO for tables converted to the Propaceous format. The Ar 'leos180' local-thermal equilibrium (LTE) EOS and opacity table with electron conductivity is used in the results presented here. This table was selected over the '5173' sesame table, which evolved to Ar^{+18} nearly immediately in the simulations. Because the gas temperature and velocity depend significantly on table accuracy, other available tables will be investigated in follow-on studies.

The resolution and code requirements for each particle treatment are presented below.

0.3.1. Quasi-neutral 1D Ar gas puff

The quasi-neutral simulations use an Eulerian remap to restore the value of one particle per cell after each time step. While this remap has been associated with numerical diffusion, none is observed in the 1D tests when using $\Delta r = 10,\ 20,\ 50\ \mu$m and $\omega_{ce}\Delta t = 1$.

The gas implosion is demonstrated in Fig. 0-3. The electron densities, shown in red, are determined by the EOS. The initial, low $\bar{Z}$ state is seen in Fig. 0-3a. However, by 10 ns (Fig. 0-3b) the electron population in the bulk of the stationary gas has increased. This must be the result of radiation transport and will be reviewed as the EOS table is further vetted.

The EOS table is also responsible for the opacities that contribute to the total radiation energy loss plotted in Fig. 0-4. This loss increases as the plasma collapses on axis, but this pinch behavior is omitted in Fig. 0-4 for questions of accuracy. The radiation transport and plasma pressure will be included in the future pinch-resolution studies.

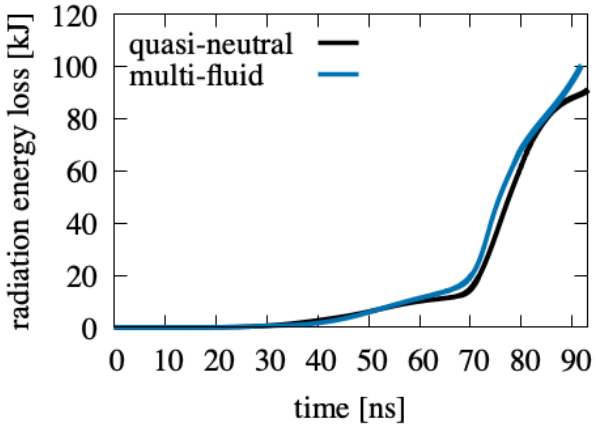

Figure 0-4. Total radiation energy loss in the quasi-neutral and multi-fluid 1D simulations.

In the quasi-neutral simulations, the implosion dynamics are convergent with cell sizes of $\Delta r = 50$, 20, and 10 μm and $\omega_{ce}\Delta t = 1$. This enables gas puff implosions to be resolved more coarsely at larger radii, before the particles transition to multi-fluid or kinetic. However, the dynamics of the pinch are likely not captured with $\Delta r = 10$ μm. The resolution required within $r \lesssim 3$ mm will be investigated in follow-on studies in conjunction with the requirements of multi-fluid and kinetic.

0.3.2. Multi-fluid 1D Ar gas puff

The multi-fluid simulations are run with an Eulerian remap, an EOS, and radiation transport, similar to the quasi-neutral simulations as show in Fig. 0-4. There are a number of fluid parameters, such as the viscosity in Eq. 0.8, that are typically tuned for z-pinch load modeling. We have reviewed and removed the viscosity and minimized the other diffusive streaming parameter. It was determined that these parameters do not enable coarser resolution. The impact of the Eulerian remap will be investigated in a follow-on study.

The multi-fluid simulation shown in Fig. 0-5 has $\Delta r = 10$ μm and $\omega_{ce}\Delta t = 1$. The resolution study is in progress with the diffusive fluid parameters removed.

0.3.3. Kinetic 1D Ar gas puffs

The kinetic particles are incompatible with an EOS treatment because the EOS assumes local thermalization and Maxwell energy distributions. The kinetic alternative is to model ionization as

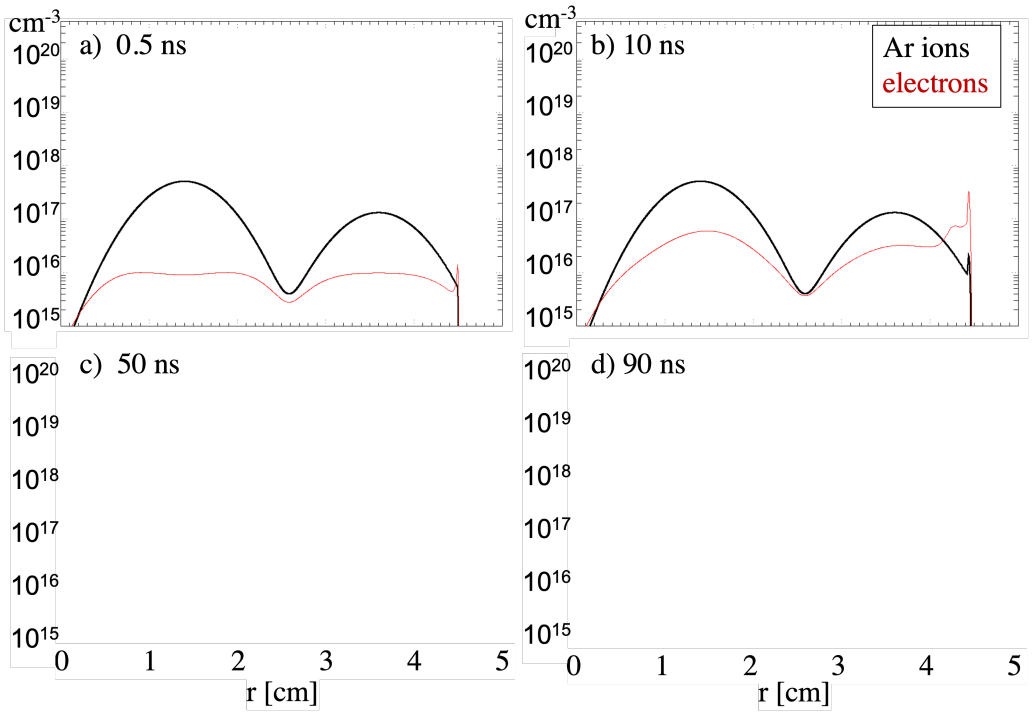

Figure 0-5. The evolution of Ar ion and electron densities in a 1D multi-fluid simulation. The density distributions are shown separately for ions (black) and electrons (red) at four times during the pinch: a) 0.5, b) 10, c) 50, and d) 90 ns.

an additional particle interaction to the Coulomb collisions in Eq. 0.1. Interaction tables are constructed for use in CHICAGO which include cross sections for elastic scattering with neutrals, momentum transfer, and impact ionization. Photoionization is also available.

This kinetic ionization treatment is not used in this study. It is computationally expensive because, in addition to the calculation of each interaction, each resulting ionization state must be tracked separately. This is beyond the scope of the current study which aims only to determine required resolution. Instead, multiple kinetic 1D simulations, with static $\bar{Z}$ of 1, 2, and 6 are conducted. So while energy distributions and collisions are more accurately (discretely) represented, the ionization states and, hence, conductivity are over-simplified.

The kinetic simulations of Ar^{+}, Ar^{2}, and Ar^{6} demonstrate the energy and spatial distributions for interpenetrating electrons and ions, which is an advantage over fluid treatments. They also demonstrate the increased spatial resolution required and the electron density increases with $\bar{Z}$. The Ar^{+} and Ar^{2} simulations are stable with $\Delta r = 5\ \mu$m and $\omega_{ce}\Delta t = 1.5$. Ar^{6} required $\Delta r = 0.5\ \mu$m to resolve the electron densities during implosion.

The densities from the Ar^{2} simulation are shown in Fig. 0-6. The distributions are analogous to those in Fig. 0-3 but with the fixed ion-electron ratio. The plots in Fig. 0-6 also show the cell-to-cell fluctuations that are a hallmark of kinetic models.

The static values of $\bar{Z}$ impact the implosion velocities, which are plotted in Fig. 0-7 as functions

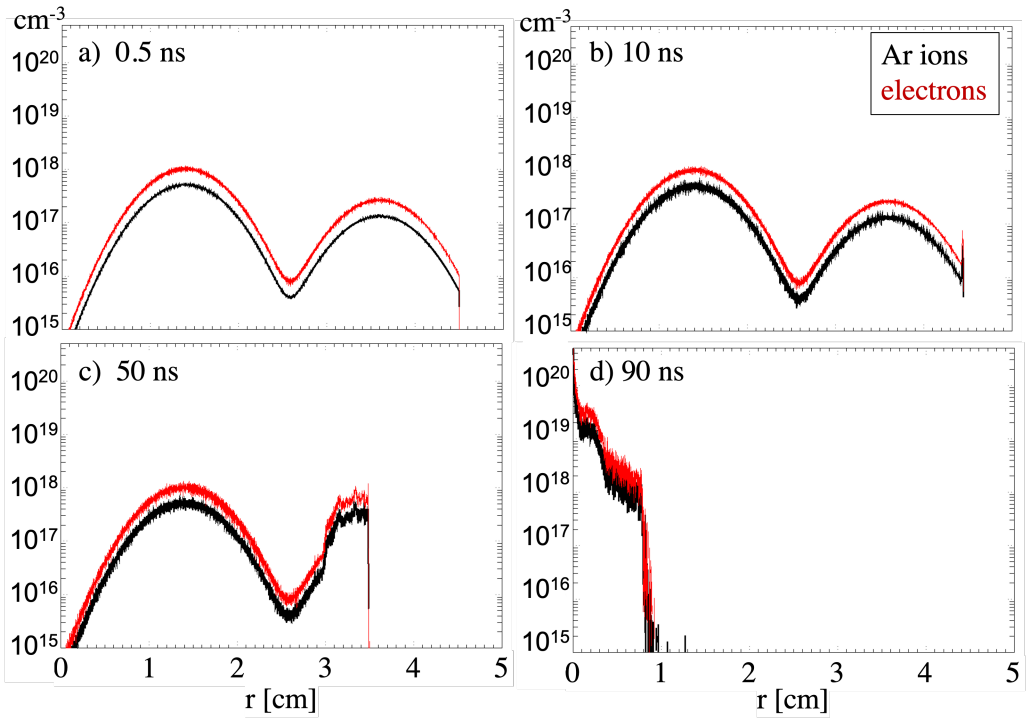

Figure 0-6. The evolution of Ar ion and electron densities in a 1D kinetic simulation initialized to Ar^{2+}. The density distributions are shown separately for ions (black) and electrons (red) at four times during the pinch: a) 0.5, b) 10, c) 50, and d) 90 ns.

of time for each simulation. A modest increase in average v_r is noted in Fig. 0-7 as $\bar{Z}$ is increased. The reversal of the accelerations in the figure is a result of the fast pulse rise, which plateaus at 69 ns while the mass swept up is increasing. This is expected to delay the pinch, as shown in Fig. 0-6d.

0.4. Physics identified in the kinetic Ar gas puff

The drawbacks of the kinetic model, at present, are the omission of the $\bar{Z}$ and radiation transport calculations. These impact the velocity, temperature, and, hence, conditions during pinch. Nonetheless, the 1D kinetic simulations highlight some important physics that is not captured in an MHD model of a z-pinch load. The results generate more realistic particle interpenetration, non-Maxwellian distributions, and collisionality. This physics is expected to impact warm x-ray targets, as detailed below.

In a kinetic simulation, the velocity distributions are discrete. Therefore, the ions in the leading edge of the plasma, referred to here as the sheath, are subject to discrete $\mathbf{v} \times \mathbf{B}$ forces. This creates a spatially varying kinetic energy distribution as ions with higher initial v_z achieve a higher final $-v_r$ at each time step. As the current increases in time, the final $-v_r$ also increases. Using the 1D simulations in Sec. 0.3.3, snapshots of the spatial distributions of Ar^+ kinetic energy $(\gamma - 1)$ are

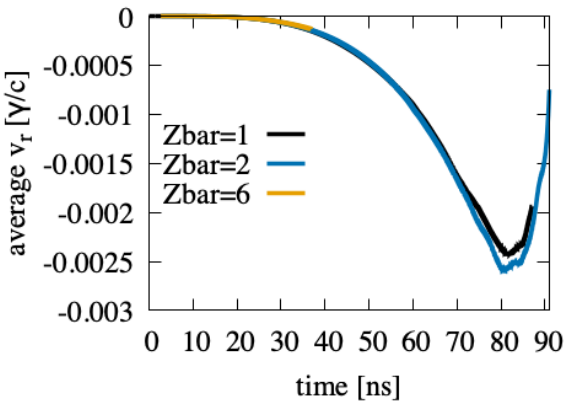

Figure 0-7. $\langle v_r \rangle$ as a function of time from 1D kinetic simulations of Ar^{+}, Ar^{2+}, and Ar^{6+}. Velocity units are γ/c.

shown in Fig. 0-8. Figures 0-8a and b show lower energy ions, those accelerated first, penetrating deeper into the gas, with higher energy ions nearer the sheath. These persists through the pulse rise. Figures 0-8a and b show that distributions during peak power have transitioned to more uniform in energy with the highest energy ions throughout the gas.

The net result is that as the plasma implodes, higher energy ions from the sheath penetrate the colder gas. The stationary gas is heated through radiation transport, and this interpenetration may heat it further.

The non-Maxwellian distributions suggested for Ar^{+} in Fig. 0-8 are determined here for electrons. The electron energies are recorded in the first mm of the sheath to capture just the accelerated electrons. Figure 0-9 plots the energy distributions at 50, 60, 70, and 80 ns into the implosion. The energy distribution is increasingly poorly defined by a Maxwell distribution as the high-energy tails are increasingly populated. This high-energy tail is predicted to be responsible for warm x-ray production [19].

The criteria for transitioning from the multi-fluid to the kinetic treatment may also be explored with the 1D simulations from Sec. 0.3.3. While more extensive analysis of criteria, such as the Dreicer field and Hall parameter, will be conducted in a follow-on study, a preliminary study of the Hall parameter shows potential for discriminating between thermal and non-thermal particle populations.

The Hall parameter (ω_c/ν_c) is calculated as a function of radius and time for the Ar^{+} and Ar^{2+} simulations in Sec. 0.3.3. The collision frequency is calculated using Eq. 0.5 with the cell-averaged electron and ion temperatures. The magnetic field in each cell is used to calculate the local ω_c. The radial distributions of ν_c and ω_c are plotted for a single snapshot in time (45 ns) in Fig. 0-10.

Figures 0-10a and b show that mobility is dominated by the electron mass. The differences in $\bar{Z}$ between Figs. 0-10a and b is negligible on the log scale. The physics that creates the contrast in Fig. 0-10 is the $\mathbf{v} \times \mathbf{B}$ sweep of particles into the colder plasma, shown in Fig. 0-8. The values of ν_c in the sheath ($r \sim 3.65$ cm in the figure) are below the minimum scale value. However, the

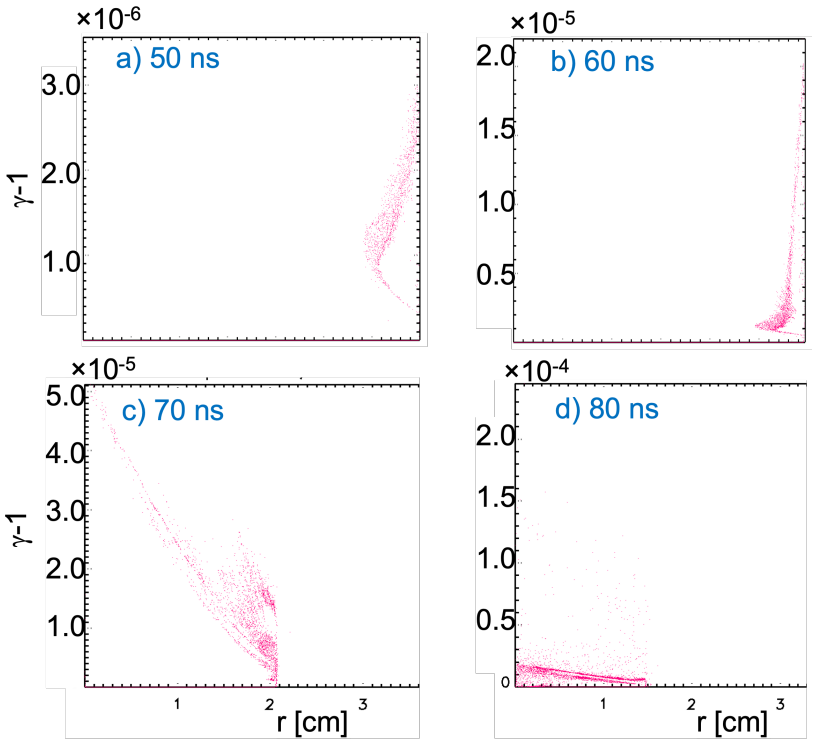

Figure 0-8. Distributions of ion kinetic energy, recorded as $\gamma - 1$, versus r for a Ar^+ plasma. Distributions are shown at a) 50 ns, b) 60 ns, c) 70 ns, and d) 80 ns into the implosion.

region behind the sheath ($r \sim 3.1 - 3.6$ cm) has a non-negligible ν_c which is a result of the hotter, accelerated particles mixing with the colder plasma. The interior plasma ($r < 3.1$ cm) remains cold and highly collisional, with a small cyclotron frequency.

The differences in the electron and ion mobility are stark in Fig. 0-10 because both ν_c and ω_c are (essentially) linear in mass. However, the mass dependencies cancel in ω_c/ν_c so only the $\bar{Z}$ differences appear in Fig. 0-11. The distinct regions of sheath, mix, and cold plasma in Fig. 0-10 are also visible in Fig. 0-11. The Hall parameter is seen to vary by many orders of magnitude between regions, providing conclusive discrimination between thermal and non-thermal populations. It is also possible that either ν_c or ω_c alone may identify the non-thermal populations of accelerated particles during an implosion.

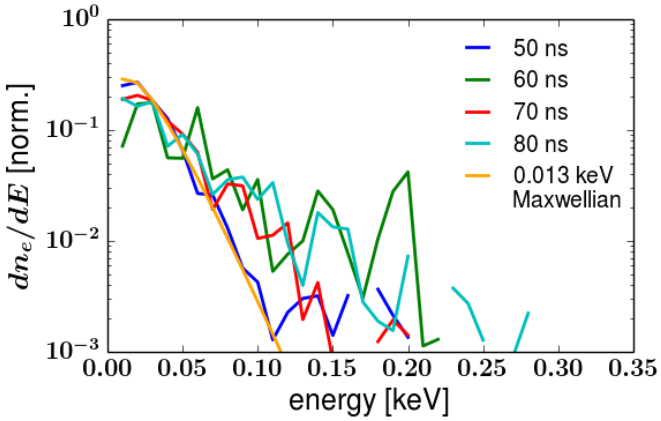

Figure 0-9. Kinetic distributions of electron energy within 1 mm of the edge of the plasma for the Ar^+ 1D simulation. Distributions are shown at four times during the implosion. A 0.013-keV Maxwellian is shown for reference.

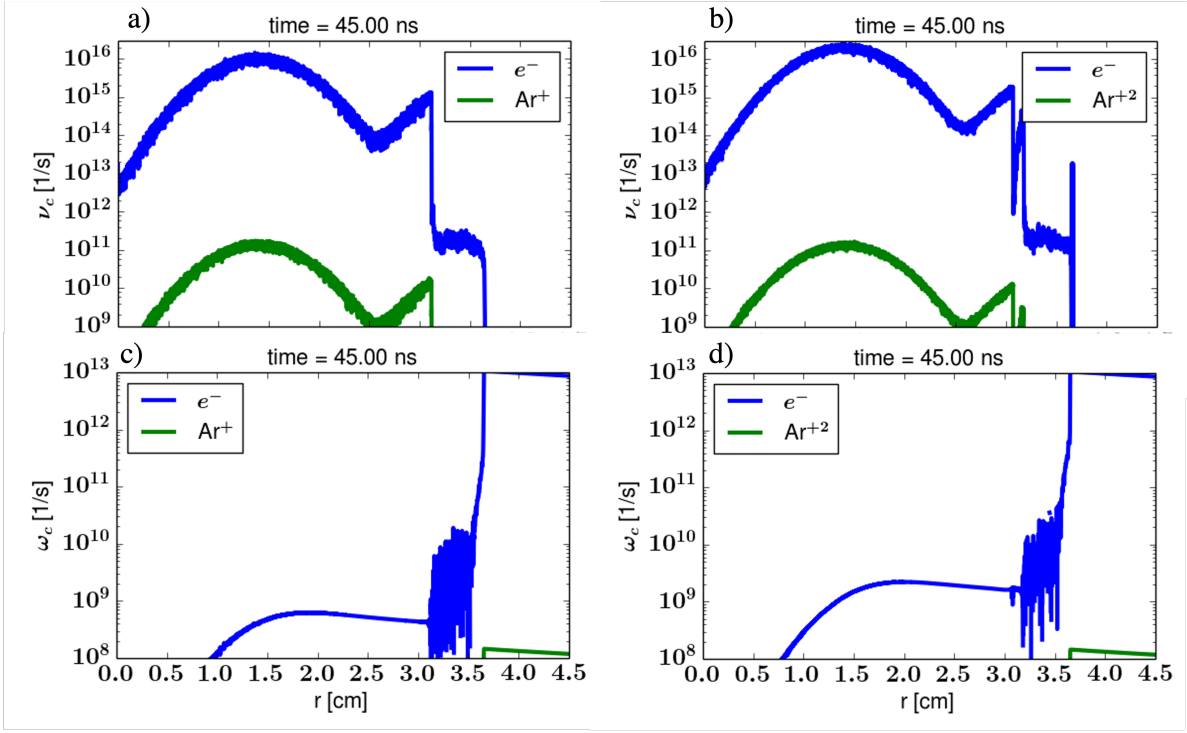

Figure 0-10. The radial distribution of ν_c and ω_c for a) Ar^+ and b) Ar^{2+} at 45 ns into the 1D simulations.

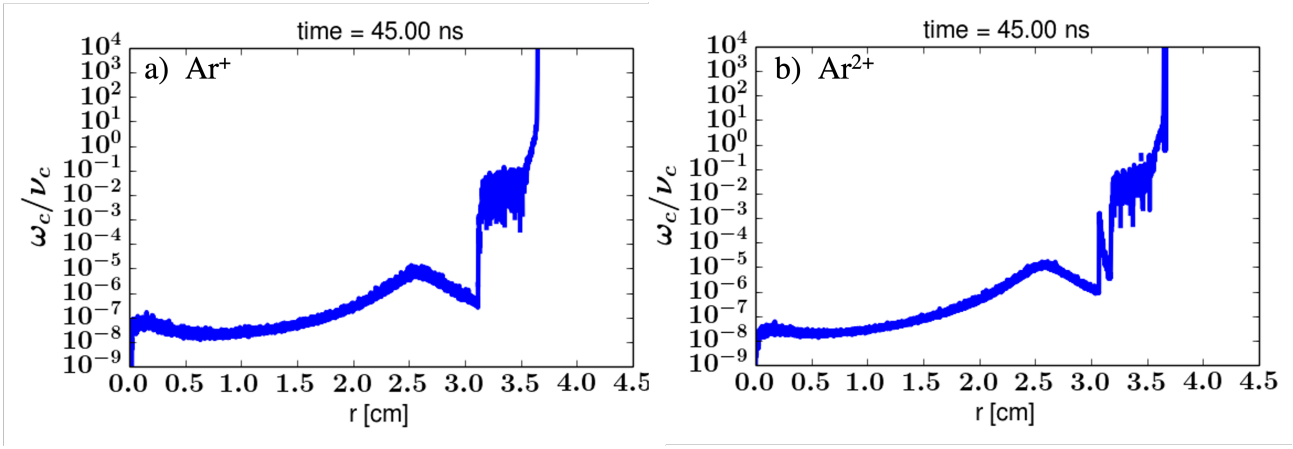

Figure 0-11. The radial distribution of the Hall parameter (ω_c/ν_c) for a) Ar^+ and b) Ar^{2+} at 45 ns into the 1D simulations.

0.5. CHICAGO code development

There are two particle migration models available in CHICAGO to transition between the particle equations of motion. One is a transition of individual particles as they exceed a directed or thermal energy threshold [36, 7] and he other is an en masse transition for all particles from one treatment to another [5]. The individual migration model required no new development. This algorithm may now be specified for multiple ion species within a single simulation. This final feature will likely be required in models of a non-thermal warm x-ray source.

The en masse migration was initially strictly implemented to receive particle species in a prescribed order and to migrate a quasi-neutral particle to a single kinetic species. This has been made more general to enable transitions to multiple ion species based on a specified fractional split, and the recipient species may be kinetic or multi-fluid. There is also no longer a prescribed order. Instead, the code searches for the appropriate ion/electron pairs as recipient species based on the ion's equation of motion.

The EOS algorithm was modified to enable a single table to describe multiple ion species. This is solely for defining a single physical ion as both multi-fluid and quasi-neutral. Maintaining charge conservation is more difficult in the multi-fluid treatment as ions change $\bar{Z}$ and this charge must be scattered to surrounding electrons. The Eulerian remap mitigates this problem by essentially creating a more matched pair of electron and ion macroparticles. The electron associated with the two ion equations of motion have been deconflicted.

A complete model of a non-thermal warm x-ray source may require the execution of both particle migration models in a single simulation. The combination of en masse and individual transitions in a single simulation has not been tested. Examples of the individual transitions are presented in Sec. 0.6.

0.6. Ar gas puff 1D models with transitions in the equations of motion

The 1D quasi-neutral simulation plotted in Fig 0-3 is modified here to transition the quasi-neutral particles en masse to multi-fluid. The migration switch time in CHICAGO is arbitrarily set to 49 ns. The particle densities before and after the transition are plotted in Fig. 0-12. The quasi-neutral electron species, which have no equation of motion, become a separate fluid species, with inertia, after the transition.

The smoothness of the transition is demonstrated in the densities in Fig. 0-12 and the total ion kinetic energies in Fig. 0-13. It should be noted that the en-masse transition was only previously demonstrated for quasi-neutral to kinetic [5].

The transition of individual particles as they exceed an energy threshold is tested for multi-fluid to kinetic. This technique has been expanded to be more versatile since it was last published [7]. This transition in CHICAGO may now be triggered on kinetic energy, perveance, fluid temperature, or the kinetic-to-thermal energy ratio. Only kinetic energy is tested here. The transition criterion ultimately selected will be based on an analysis of kinetic distributions, similar to those in Sec. 0.4.

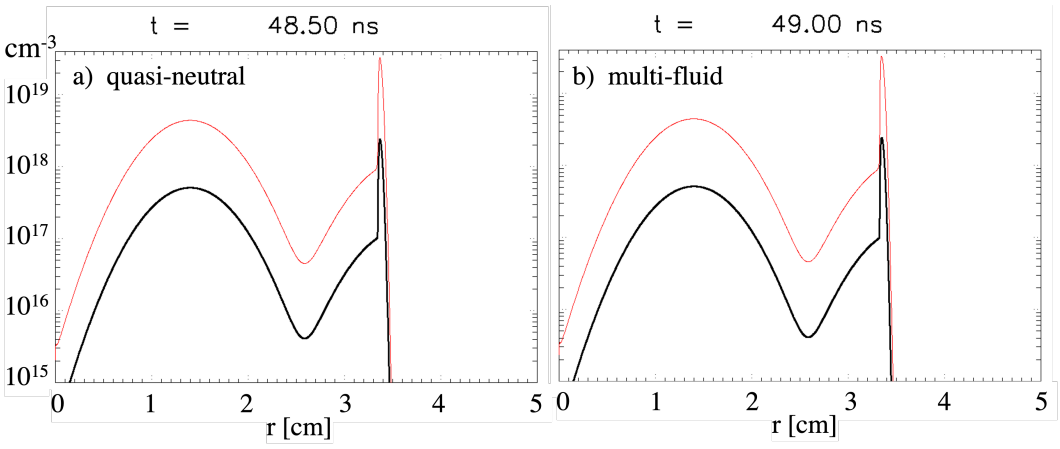

Figure 0-12. The Ar ion and electron densities in a 1D simulation in which the particles transition from a) quasi-neutral to b) multi-fluid en masse at 49.0 ns.

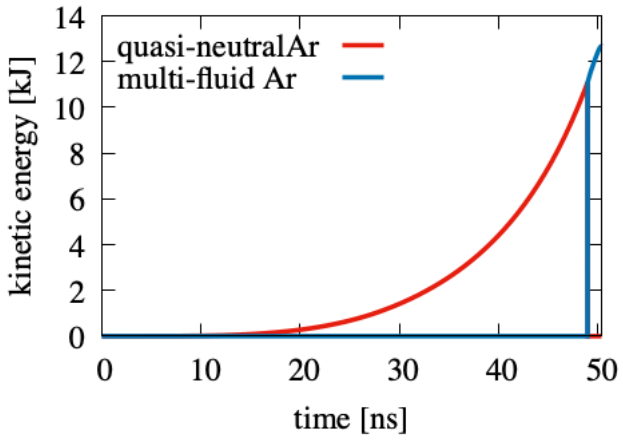

Figure 0-13. Total Ar ion kinetic energy in a 1D simulation in which the particles transition from quasi-neutral (red) to multi-fluid (blue) en masse at 49.0 ns.

For the transition test shown in Fig. 0-14, the EOS treatment has been removed so the kinetic electrons are not under-resolved. The resolution is 10μm, sufficient for the initial implosion. The kinetic ions are seen to transition in the sheath, which may be a requirement for a gas puff model.

0.7. 2D model of the Ar gas puff shot z2559

A more realistic model of an Ar gas puff is performed in 2D quasi-neutral to establish the framework for future shot modeling. The shot uses a realistic driving pulse created by the BERTHA circuit model of a Z forward-going wave [21, 6] at 85-kV Marx charge. The simulation is based on the published gas shell distributions from an 8-cm-diameter nozzle [25] emitting two

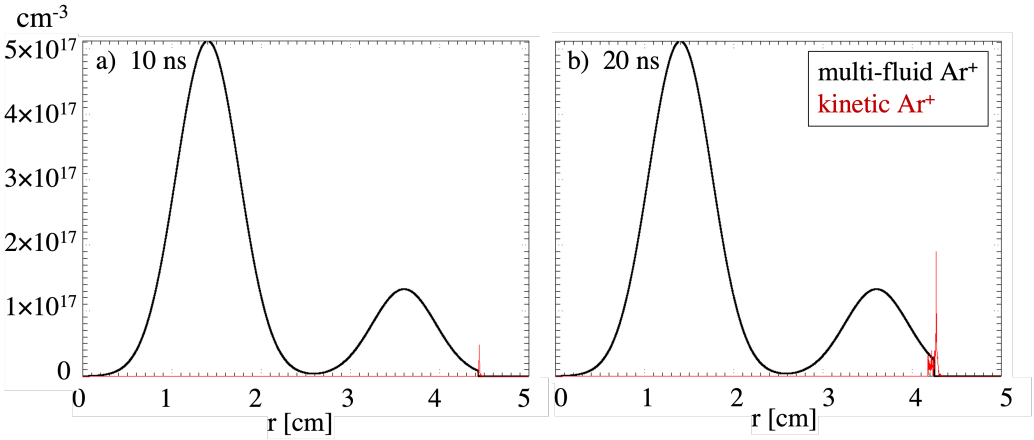

Figure 0-14. Ar^+ densities with transitions enabled from multi-fluid (black) to kinetic (red). The number of particles transitioning increases with the pulse rise from a) 10 ns to b) 20 ns.

concentric annular shells with outer-to-inner shell mass ratios of 1:1.6 [24, 20]. Among the Z shots that use this configuration are z2381 at 70-kV Marx charge, and z2559, z2560, and z2561 at 85-kV Marx charge. The gas density distribution used during implosion is determined from a GORGON [11] hydrodynamic simulation of the flow of gas from the nozzle with constant pressure until steady-state is reached [22]. This steady-state gas distribution, with the MHD floor density, is shown in Fig. 0-15.

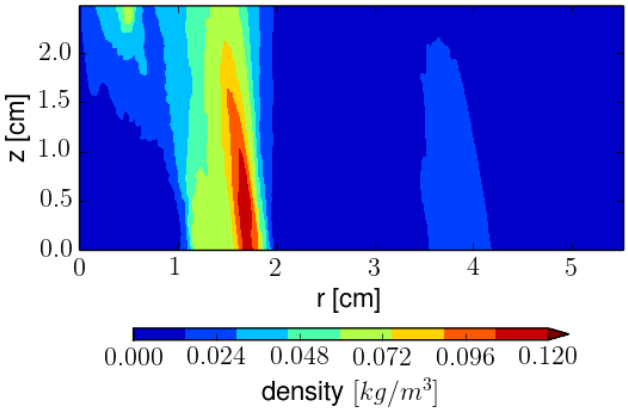

Figure 0-15. The gas density distribution in a 2-shell Ar gas puff determined from a GORGON hydrodynamic model [11] of the gas nozzle with two concentric annular shells [22].

The gas distribution in Fig. 0-15, without the floor density, initializes the 2D CHICAGO simulation. This simulation uses $\Delta r, z = 20\ \mu$m and $\omega_{ce}\Delta t = 3.0$. Gas breakdown and radiation transport are modeled using the Ar 'leos180' LTE EOS and opacity table. The resulting evolution of the Ar ion and electron densities are illustrated in Fig. 0-16 which shows the density contours

of both species at 0 and 6.4 MA (60 ns) into the simulation. The bulk value of $\bar{Z}$ at 60 ns is ~ 5 in the inner shell, ~ 5 in the outer shell, and 11-14 in the sheath.

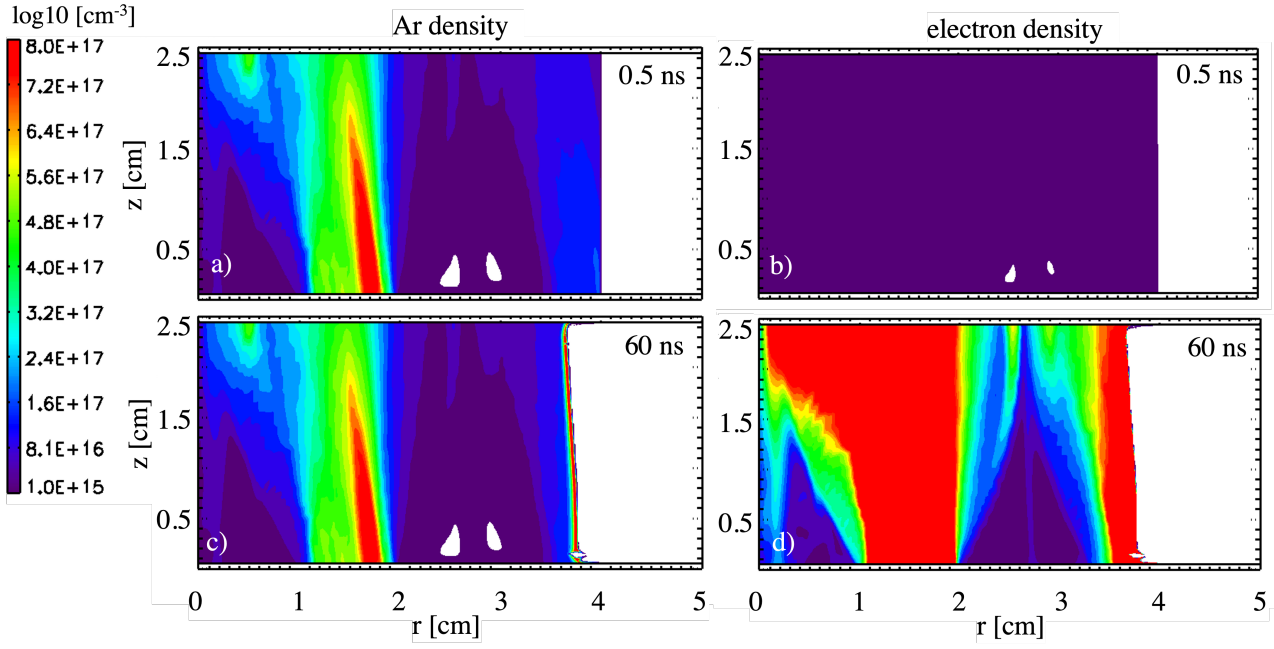

Figure 0-16. The Ar ion and electron density distributions in a 2D quasi-neutral simulation of shot z2381. The Ar ion densities are shown at left for a) 0.5 ns and c) 60 ns. The electron densities are shown at right for b) 0.5 ns and d) 60 ns.

Preliminary results from the 2D simulation suggest the major issue for modeling gas puff targets is the combined large volume (196.3 cm^3) and high spatial resolution (1,875,000 grid cells). The spatial and temporal resolutions will increase as particle transitions and load physics are introduced to the simulations. Therefore, load simulations will be more efficiently modeled on the large capacity computing platforms.

0.8. Conclusion

We have reported on a six-month research effort to advance the hybrid kinetic-fluid modeling capability required for developing non-thermal warm x-ray sources on Z. This research effort focused on a model of an Ar gas puff [20] accomplishing four tasks. First, the three particle treatments of quasi-neutral, multi-fluid, and kinetic were exercised on a 1D model of the Ar gas puff. This determined particle resolution requirements. Second, the 1D models were used to test transitions between the particle treatments. Third, kinetic 1D simulations demonstrated the energy and spatial distributions for interpenetrating electrons and ions. These also demonstrated the utility of the Hall parameter as a transition criterion. Fourth, a 2D Ar gas puff simulation establishes the capability for modeling with realistic pulse-power and gas-nozzle configurations.

We identified items as incomplete from this six-month project that will be addressed in a follow-on study. These include

- the required resolution in the pinch region,
- the diffusivity of the Eulerian remap,
- other EOS/opacity tables, and
- an extensive analysis of particle treatment transition criteria, such as the Dreicer field and Hall parameter.

The gas pinch temperature and velocity depend significantly on the opacities and conductivities provided by the EOS tables, and some table inaccuracies were discovered in testing. Therefore, other available Ar tables will be investigated in the future.

A complete model of a non-thermal warm x-ray source will require the execution of both particle migration models in a single simulation. The combination of en masse and individual transitions in a single simulation has not been tested.

In addition to the unfinished analyses in this research effort, a future LDRD will investigate

- the maximum allowable $\omega_{ce}\Delta t$,
- the nature of artificial collisionality and the role of fluid streaming parameters in load modeling,
- the most stable cloud-in-cell function, and
- the resolution required for wire arrays and advanced x-ray sources.

The tasks that have been accomplished increase confidence that we can develop a modeling capability for developing improved warm x-ray sources. The incomplete tasks listed above are in the scope of a future LDRD. Additionally, we will continue model development for transitions between the particle treatments and connections to a non-local thermal equilibrium look-up table for estimating the warm x-ray yields.

REFERENCES

[1] D. J. Ampleford, S. B. Hansen, C. A. Jennings, B. Jones, C. A. Coverdale, A. J. Harvey-Thompson, G. A. Rochau, G. Dunham, N. W. Moore, E. C. Harding, M. E. Cuneo, Y.-K. Chong, R. W. Clark, N. Ouart, J. W. Thornhill, J. Giuliani, and J. P. Apruzese. Opacity and gradients in aluminum wire array z-pinch implosions on the z pulsed power facility. *Phys. Plasmas*, 21(3):031201, 2014.

[2] D. J. Ampleford, C. A. Jennings, B. Jones, S. B. Hansen, M. E. Cuneo, C. A. Coverdale, M. C. Jones, T. M. Flanagan, M. Savage, W. A. Stygar, M. R. Lopez, J. P. Apruzese, J. W. Thornhill, J. L. Giuliani, and Y. Maron. K-shell emission trends from 60 to 130âĂŁcm/μs stainless steel implosions. *Phys. Plasmas*, 20(10):103116, 2013.

[3] David J. Ampleford, Stephanie B Hansen, Christopher A Jennings, Timothy J. Webb, Victor Harper-Slaboszewicz, Guillaume P. Loisel, Timothy M. Flanagan, Kate S. Bell, Brent Jones, Leroy A. McPherson, Gregory A. Rochau, Jeremy P. Chittenden, Mark Sherlock, Brian Appelbe, John Giuliani, Nicholas Ouart, and John Seely. Non-thermal x-ray emission from wire array z-pinches. Technical Report SAND2015-10453, Sandia National Laboratories, 2015.

[4] R. Balescu. *Transport Processes in Plasmas*. North Holland, Amsterdam, 1988.

[5] N. Bennett, M. Blasco, K. Breeding, D. Constantino, A. DeYoung, V. DiPuccio, J. Friedman, B. Gall, S. Gardner, J. Gatling, E. C. Hagen, A. Luttman, B. T. Meehan, M. Misch, S. Molnar, G. Morgan, R. O'Brien, L. Robbins, R. Rundberg, N. Sipe, D. R. Welch, and V. Yuan. Development of the dense plasma focus for short-pulse applications. *Phys. Plasmas*, 24(1):012702, 2017.

[6] N. Bennett, D. R. Welch, C. A. Jennings, E. Yu, M. H. Hess, B. T. Hutsel, G. Laity, J. K. Moore, D. V. Rose, K. Peterson, and M. E. Cuneo. Current transport and loss mechanisms in the *z* accelerator. *Phys. Rev. Accel. Beams*, 22:120401, Dec 2019.

[7] Nichelle Bennett, Dale R. Welch, Timothy J. Webb, Michael G. Mazarakis, Mark L. Kiefer, M. Dale Crain, Darryl W. Droemer, Raymond E. Gignac, Mark D. Johnston, Joshua J. Leckbee, Isidro Molina, Dan Nielsen, Robert Obregon, Tobias Romero, Sean Simpson, Chase C. Smith, Frank L. Wilkins, and Derek Ziska. The impact of plasma dynamics on the self-magnetic-pinch diode impedance. *Phys. Plasmas*, 22(3):033113, 2015.

[8] C. K. Birdsall and A. B. Langdon. *Plasma Physics via Computer Simulation*. Adam Hilger, New York, 1991.

[9] T.J.M. Boyd and J.J. Sanderson. *The Physics of Plasmas*. Cambridge University Press, 2003.

[10] S. I. Braginskii. Transport Processes in a Plasma. In M. A. Leontovich, editor, *Reviews of Plasma Physics*, volume 1, page 205. Consultants Bureau, New York, 1965.

[11] J P Chittenden, S V Lebedev, C A Jennings, S N Bland, and A Ciardi. X-ray generation mechanisms in three-dimensional simulations of wire array z-pinches. *Plasma Phys. Contr. Fus.*, 46(12B):B457–B476, nov 2004.

[12] C.A. Coverdale, K.S. Bell, T.M. Flanagan, N. W. Moore, V. Harper-Slaboszewicz, B. Ulmen, D.J. Ampleford, L.A. McPherson, G. Loisel, and G. Laity. Warm x-ray platform work on the z machine: Radiation effects test objects and diagnostic development. Technical Report SAND2017-1396, Sandia National Laboratories, 2017.

[13] C.A. Coverdale, B. Jones, D.J. Ampleford, J. Chittenden, C. Jennings, J.W. Thornhill, J.P. Apruzese, R.W. Clark, K.G. Whitney, A. Dasgupta, J. Davis, J. Guiliani, P.D. LePell, C. Deeney, D.B. Sinars, and M.E. Cuneo. K-shell x-ray sources at the z accelerator. *High Energy Density Physics*, 6(2):143–152, 2010. ICHED 2009 - 2nd International Conference on High Energy Density Physics.

[14] M. E. Cuneo, D. B. Sinars, E. M. Waisman, D. E. Bliss, W. A. Stygar, R. A. Vesey, R. W. Lemke, I. C. Smith, P. K. Rambo, J. L. Porter, G. A. Chandler, T. J. Nash, M. G. Mazarakis, R. G. Adams, E. P. Yu, K. W. Struve, T. A. Mehlhorn, S. V. Lebedev, J. P. Chittenden, and C. A. Jennings. Compact single and nested tungsten-wire-array dynamics at 14âĂŞ19MA and applications to inertial confinement fusion. *Phys. Plasmas*, 13(5):056318, 2006.

[15] H. Dreicer. Electron and ion runaway in a fully ionized gas. i. *Phys. Rev.*, 115:238–249, Jul 1959.

[16] H. Dreicer. Electron and ion runaway in a fully ionized gas. ii. *Phys. Rev.*, 117:329–342, Jan 1960.

[17] B. Jones *et al.* Advanced k-shell radiation sources for radiation effects sciences on Z. Technical Report SAND2012-8150, Sandia National Laboratories, 2012.

[18] T. C. Genoni, R. E. Clark, and D. R. Welch. A fast implicit algorithm for highly magnetized charged particle motion. *The Open Plasma Physics Journal*, 3:36, 2010.

[19] S. B. Hansen, D. J. Ampleford, M. E. Cuneo, N. Ouart, B. Jones, C. A. Jennings, A. Dasgupta, C. A. Coverdale, G. A. Rochau, G. Dunham, J. L. Giuliani, and J. P. Apruzese. Signatures of hot electrons and fluorescence in mo kÎś emission on z. *Phys. Plasmas*, 21(3):031202, 2014.

[20] A. J. Harvey-Thompson, C. A. Jennings, B. Jones, J. P. Apruzese, D. J. Ampleford, D. C. Lamppa, C. A. Coverdale, M. E. Cuneo, J. L. Giuliani, S. B. Hansen, M. C. Jones, N. W. Moore, G. A. Rochau, and J. W. Thornhill. Investigating the effect of adding an on-axis jet to ar gas puff z pinches on z. *Phys. Plasmas*, 23(10):101203, 2016.

[21] B. T. Hutsel, P. A. Corcoran, M. E. Cuneo, M. R. Gomez, M. H. Hess, D. D. Hinshelwood, C. A. Jennings, G. R. Laity, D. C. Lamppa, R. D. McBride, J. K. Moore, A. Myers, D. V. Rose, S. A. Slutz, W. A. Stygar, E. M. Waisman, D. R. Welch, and B. A. Whitney.

Transmission-line-circuit model of an 85-tw, 25-ma pulsed-power accelerator. *Phys. Rev. Accel. Beams*, 21:030401, Mar 2018.

[22] C. A. Jennings, D. J. Ampleford, D. C. Lamppa, S. B. Hansen, B. Jones, A. J. Harvey-Thompson, M. Jobe, T. Strizic, J. Reneker, G. A. Rochau, and M. E. Cuneo. Computational modeling of krypton gas puffs with tailored mass density profiles on z. *Phys. Plasmas*, 22(5):056316, 2015.

[23] Brent Jones, Christine A. Coverdale, Christopher Deeney, Daniel B. Sinars, Eduardo M. Waisman, Michael E. Cuneo, David J. Ampleford, P. David LePell, Kyle R. Cochrane, J. Ward Thornhill, J. P. Apruzese, Arati Dasgupta, Kenneth G. Whitney, Robert W. Clark, and Jeremy P. Chittenden. Implosion dynamics and k-shell x-ray generation in large diameter stainless steel wire array z pinches with various nesting configurations. *Phys. Plasmas*, 15(12):122703, 2008.

[24] Brent Jones, Christopher A. Jennings, Derek C. Lamppa, Stephanie B. Hansen, Adam J. Harvey-Thompson, David J. Ampleford, Michael E. Cuneo, Thomas Strizic, Drew Johnson, Michael C. Jones, Nathan W. Moore, Timothy M. Flanagan, John L. McKenney, Eduardo M. Waisman, Christine A. Coverdale, Mahadevan Krishnan, Philip L. Coleman, Kristi Wilson Elliott, Robert E. Madden, John Thompson, Alex Bixler, J. Ward Thornhill, John L. Giuliani, Young K. Chong, Alexander L. Velikovich, Arati Dasgupta, and John P. Apruzese. A renewed capability for gas puff science on sandia's z machine. *IEEE Trans. Plasma Sci.*, 42(5):1145–1152, 2014.

[25] Mahadevan Krishnan, Kristi Wilson Elliott, Robert E. Madden, P. L. Coleman, John R. Thompson, Alex Bixler, D. C. Lamppa, J. L. McKenney, T. Strizic, D. Johnson, O. Johns, M. P. Vigil, B. Jones, D. J. Ampleford, M. E. Savage, M. E. Cuneo, and M. C. Jones. Architecture, implementation, and testing of a multiple-shell gas injection system for high current implosions on the z accelerator. *Rev. Sci. Instru.*, 84(6):063504, 2013.

[26] George R. Laity, Allen C. Robinson, Michael E. Cuneo, M. Kathleen Alam, Kristian R. C. Beckwith, Nichelle L. Bennett, Matthew T. Bettencourt, Stephen D. Bond, Kyle Cochrane, Louise Criscenti, Eric C. Cyr, Karen De Zetter, Richard R. Drake, Evstati G. Evstatiev, Andrew S. Fierro, Thomas A. Gardiner, Forrest W. Glinesa, Ronald S. Goeke, Nathaniel D. Hamlin, Russell Hooper, Jason Koski, J. Matthew Lane, Steven R. Larson, Kevin Leung, Duncan A. McGregor, Philip R. Miller, Sean M. Miller, Susan J. Ossareh, Edward G. Phillips, Nicholas A. Roberds, Charles E. Rose, John N. Shadid, Sidney Shields, Sean C. Simpson, David Sirajuddina, Thomas M. Smith, M. Scot Swan, Aidan P. Thompson, and Julien G. Tranchida. Towards predictive plasma science and engineering through revolutionary multi-scale algorithms and models, final report. Technical Report SAND2021-0718, Sandia National Laboratories, 2021.

[27] P. W. Rambo and R. J. Procassini. A comparison of kinetic and multifluid simulations of laserâĂŘproduced colliding plasmas. *Phys. Plasmas*, 2(8):3130–3145, 1995.

[28] H. Sze, P. L. Coleman, J. Banister, B. H. Failor, A. Fisher, J. S. Levine, Y. Song, E. M. Waisman, J. P. Apruzese, R. W. Clark, J. Davis, D. Mosher, J. W. Thornhill, A. L. Velikovich, B. V. Weber, C. A. Coverdale, C. Deeney, T. L. Gilliland, J. McGurn, R. B.

Spielman, K. W. Struve, W. A. Stygar, and D. Bell. Efficient argon k-shell radiation from a z pinch at currents >15 ma. *Physics of Plasmas*, 8(7):3135–3138, 2001.

[29] C. Thoma, D. R. Welch, R. E. Clark, N. Bruner, J. J. MacFarlane, and I. E. Golovkin. Two-fluid electromagnetic simulations of plasma-jet acceleration with detailed equation-of-state. *Phys. Plasmas*, 18(10):103507, 2011.

[30] C. Thoma, D. R. Welch, R. E. Clark, D. V. Rose, and I. E. Golovkin. Hybrid-pic modeling of laser-plasma interactions and hot electron generation in gold hohlraum walls. *Phys. Plasmas*, 24(6):062707, 2017.

[31] C. Thoma, D.R. Welch, and D.V. Rose. Implicit highly-coupled single-ion hall-mhd formulation for hybrid particle-in-cell codes. *Comp. Phys. Comm.*, 261:107823, 2021.

[32] R. Vesey, S. Hansen, and P.J. Christenson. Design and testing of warm x-ray and fast neutron sources on z to support the hostile environments gc-ldrd. Technical Report SAND2016-9852, Sandia National Laboratories, 2016.

[33] D. R. Welch, N. Bennett, T. C. Genoni, C. Thoma, and D. V. Rose. Fast hybrid particle-in-cell technique for pulsed-power accelerators. *Phys. Rev. Accel. Beams*, 23:110401, Nov 2020.

[34] D. R. Welch, N. Bennett, D.V. Rose, C. Thoma, and W.A. Stygar. Electrode contaminant plasma effects in 10^7-ampere z pinch accelerators. *Phys. Rev. Accel. Beams*, 22:070401, 2019.

[35] D. R. Welch, D. V. Rose, B. V. Oliver, E. Schamiloglu, K. Hahn, and J. E. Maenchen. Transport of a relativistic electron beam in gas and plasma-filled focusing cells for x-ray radiography. *Phys. Plasmas*, 11(2):751–760, 2004.

[36] Dale R. Welch, David V. Rose, Nichelle Bruner, Robert E. Clark, Bryan V. Oliver, Kelly D. Hahn, and Mark D. Johnston. Hybrid simulation of electrode plasmas in high-power diodes. *Phys. Plasmas*, 16(12):123102, 2009.

DISTRIBUTION

Hardcopy—Internal

Number of Copies	Name	Org.	Mailstop
1	L. Martin, LDRD Office	1910	0359

Email—External [redacted]

Name	Company Email Address	Company Name
Dale Welch	dale.welch@vosssci.com	Voss Scientific. LLC

Email—Internal [redacted]

Name	Org.	Sandia Email Address
Brent Jones	1381	bmjones@sandia.gov
Kristian Beckwith	1684	kbeckwi@sandia.gov
Nichelle Bennett	1684	nlbenne@sandia.gov
Technical Library	1911	sanddocs@sandia.gov

Sandia National Laboratories

Sandia National Laboratories is a multimission laboratory managed and operated by National Technology & Engineering Solutions of Sandia LLC, a wholly owned subsidiary of Honeywell International Inc., for the U.S. Department of Energy's National Nuclear Security Administration under contract DE-NA0003525.